The Use of Super-Resolution Techniques to Reduce Slice Thickness in Functional MRI

Ronald R. Peeters,[1] Pierre Kornprobst,[2] Mila Nikolova,[3] Stefan Sunaert,[1] Thierry Vieville,[2] Grégoire Malandain,[4] Rachid Deriche,[2] Olivier Faugeras,[2] Michael Ng,[5] Paul Van Hecke[1]

[1] Department of Radiology, KULeuven, Leuven, Belgium

[2] INRIA Sophia Antipolis, Projet Odyssée, France

[3] Département Traitement du Signal, ENST, Paris, France

[4] INRIA Sophia Antipolis, Projet Epidaure, France

[5] Department of Mathematics, The University of Hong Kong, Pokfulam, Hong Kong.

Received 15 February 2004; accepted 30 April 2004

ABSTRACT: The problem of increasing the slice resolution of functional MRI (fMRI) images without a loss in signal-to-noise ratio is considered. In standard fMRI experiments, increasing the slice resolution by a certain factor decreases the signal-to-noise ratio of the images with the same factor. For this purpose an adapted EPI MRI acquisition protocol is proposed, allowing one to acquire slice-shifted images from which one can generate interpolated super-resolution images, with an increased resolution in the slice direction. To solve the problem of correctness and robustness of the created super-resolution images from these slice-shifted datasets, the use of discontinuity preserving regularization methods is proposed. Tests on real morphological, synthetic functional, and real functional MR datasets have been performed, by comparing the obtained super-resolution datasets with high-resolution reference datasets. In the morphological experiments the image spatial resolution of the different types of images are compared. In the synthetic and real fMRI experiments, on the other hand, the quality of the different datasets is studied as function of their resulting activation maps. From the results obtained in this study, we conclude that the proposed super-resolution techniques can both improve the signal-to-noise ratio and augment the detectability of small activated areas in fMRI image sets acquired with thicker slices. © 2004 Wiley Periodicals, Inc. Int J Imaging Syst Technol, 14, 131–138, 2004; Published online in Wiley InterScience (www.interscience.wiley.com). DOI 10.1002/ima.20016

Key words: fMRI; Super-Resolution algorithm; SNR

I. INTRODUCTION

In functional magnetic resonance imaging (fMRI), a major goal is to maximize the image spatial resolution, which will allow the investigator to visualize the smallest region of neuronal brain activity (Chen and Ugurbil, 1999). To obtain high-resolution activation maps, the spatial resolution of the standard fMRI experiments performed at 1.5 T does not suffice, as the penalty for acquiring higher-resolution images is a reduction in signal-to-noise ratio (SNR) (Hoogenraad et al., 1999), which is proportional to the decrease in voxel size. This decrease in SNR can be obviated by the use of higher magnetic field scanners (Thulborn et al., 1997), but these imply an increased inhomogeneity and larger distortion artifacts in the images, present especially in fMRI (Fischer and Ladebeck, 1998; Kelley and Schenck, 1999). Another tool to enhance the resolution of the acquired MR images is the use of super-resolution techniques. These techniques can be divided into two categories. In the first, special acquisition techniques are used to obtain only partial k-space data and to model the remaining part of the data with the aid of various postprocessing techniques, (Xiong et al., 1999; Zaitsev et al., 2001). With these techniques, one can thus increase the in-plane resolution of the acquired images. The second category of super-resolution reconstruction techniques are applied in the image space after reconstruction of the raw data. With the aid of appropriate interpolation algorithms (Aizawa et al., 1991; Elad and Feuer, 1999), one is able to generate a high-resolution volume from a set of different low-resolution volumes (Carel and Zisserman, 2000; Irani and Peleg, 1993). In 2D Fourier Transform anatomical MR images this approach has been employed to increase the resolution in the image space, i.e., in the slice direction (Greenspan et al., 2002; Peled and Yeshurun, 2001; Scheffler, 2002).

In this article we focus on the applicability of the second type of techniques in fMRI experiments and propose an optimized approach for high-resolution fMRI image reconstruction using super-resolution algorithms. In this technique the fMRI acquisition is adapted to acquire different image stacks with a low slice resolution, shifted over half-a-slice thickness, generating two separate slice-shifted

Correspondence to: Ronald R. Peeters; e-mail: Ronald.Peeters@uz.kuleuven.ac.be

Grant sponsor: Research partially funded by European project MAPAWAMO (QLG3-CT-2000-30161), the Belgium Interuniversity Attraction Pole (IUAP) project (P5/04); coordinator and the Hong Kong Research Grants Council Grant No. HKU 7046/03P.

overlapping volumes, each obtained at half the acquisition time of the high-resolution volume. These shifted volumes are combined with the super-resolution algorithm, which combines recent work on edge-preserving approaches and convergence rate studies (Nikolova and Ng, 2001), to reconstruct a stack of slices with half the acquisition thickness.

First, we tested our super-resolution algorithms on morphological MR images to investigate the power of the proposed technique and to compare them with results from the literature (Greenspan et al., 2002). In the second part of the article the super-resolution reconstruction technique is utilized on real and simulated fMRI time series data to demonstrate the applicability and performance of the super-resolution technique in real fMRI experiments.

II. THE MATHEMATICAL MODEL FOR DATA ACQUISITION

Let us denote by Δ_x, Δ_y, and Δ_z the high-resolution discretization steps (voxel dimensions). In the high-resolution images; $h_{i,j,k}$ represents the intensity of the volume $W_{i,j,k}$ of each voxel of the image

$$W_{i,j,k} = [(i-1)\Delta_x, i\Delta_x] \times [(j-1)\Delta_y, j\Delta_y] \times [(k-1)\Delta_z, k\Delta_z].$$

In the low-resolution images, $l^r_{i,j,k}$ with $r = 1, \ldots, R$ represents the intensity of the volume $V^r_{i,j,k}$ of each voxel of the image

$$V^r_{i,j,k} = [(i-1)\Delta_x, i\Delta_x] \times [(j-1)\Delta_y, j\Delta_y] \times [(R(k-1)+r)\Delta_z, (Rk+r)\Delta_z].$$

Irani and Greenspan (Irani and Peleg, 1993; Greenspan et al., 2002) used a convolutional model to describe the relation between h and l^r. We, on the other hand, adopted an additive model. Namely, if $s(x)$ is the signal intensity of the nuclei located at x, the signal relevant to a volume v is $\int_v s(x)dx$. There is also measurement noise, denoted by n. Thus the intensity of the voxel at (i, j, k) in the r^{th} low-resolution image reads

$$l^r_{i,j,k} = \sum_{m=R(k-1)+r+1}^{Rk+r} \int_{V_{i,j,m}} s(x)dx + n^r_{i,j,k} = \sum_{m=R(k-1)+r+1}^{Rk+r} h_{i,j,m} + n^r_{i,j,k}. \quad (1)$$

It is convenient to put the latter relation into a matrix form. Given (i, j), let $\mathrm{h}_{i,j}$ and $\ell^r_{i,j}$ be the vectors

$$h_{i,j} = [h_{i,j,l}, \ldots, h_{i,j,p}]^T \quad (2)$$

$$l^r_{i,j} = [l^r_{i,j,l}, \ldots, l^r_{i,j,p}]^T \text{ for } r = 1, \ldots, R, \quad (3)$$

where p is the length of $h_{i,j}$ and p_r is the length of $\mathrm{l}^r_{i,j}$. Relation (1) can then be expressed as

$$\mathrm{l}^r_{i,j} = B^r h_{i,j} + n^r_{i,j}, \forall\, i, j \text{ where}$$

$$B^r_{k,n} = \begin{cases} 1 & \text{if } R(k-1)+r+1 \le n \le Rk+r \\ 0 & \text{otherwise} \end{cases}.$$

The super-resolution problem consists, therefore, in finding $\mathrm{h}_{i,j}$, for all (i, j), based on the low- resolution $\mathrm{l}^r_{i,j}$, for all r and (i, j).

III. AN EDGE-PRESERVING SUPER-RESOLUTION TECHNIQUE

The least-square solution of this problem is the minimizer $\hat{\boldsymbol{h}}$ of the following objective function

$$\Psi(h) = \sum_{i,j} \sum_{r=0}^{R-1} \|B^r h_{i,j} - \mathrm{l}^r_{i,j}\|^2 \quad (4)$$

This problem (Fischer and Ladebeck, 1998), however, is ill posed because such an $\hat{\boldsymbol{h}}$ is poor and unstable with respect to noise (Capel and Zisserman, 2000). In such cases a common approach in the field of computer vision is to add a penalty term $\Phi(h)$ on the first derivatives of h (Capel and Zisserman, 2000; Engl et al., 2000). The sought solution is defined as the minimizer $\hat{\boldsymbol{h}}$ of a penalized objective function of the form

$$J(h) = \Psi(h) + \Phi(h) \text{ with} \quad (5)$$

$$\Phi(h) = \sum_{i,j,k} (\beta_x \varphi(h_{i,j,k} - h_{i-1,j,k}) + \beta_y \varphi(h_{i,j,k} - h_{i,j-1,k}) + \beta_z \varphi(h_{i,j,k} - h_{i,j,k-1})). \quad (6)$$

The differences between the parentheses above provide an approximation of the spatial derivatives of h in the x, y and z directions, and φ: IR $\rightarrow$ IR is called a potential function. To have a convex minimization problem, we require φ to be a convex function. Different edge-preserving convex functions φ have been considered by many authors (Aubert and Kornprobst, 2002; Aubert and Vese, 1997; Geman and Yang, 1995; Rudin et al., 1992). Among them, we have chosen

$$\varphi(t) = \begin{cases} t^2/2 & \text{if } |t| \le \alpha \\ \alpha\, t - \alpha^2/2 & \text{if } |t| > \alpha \end{cases} \quad \text{(Huber function)} \quad (7)$$

because it is composed of quadratic and linear pieces and leads to simple numerical calculations. Following our acquisition procedure of shifts applied only in the slice direction, the combined data involves distortion (i.e., possible introduction of artefacts) in the z direction only. This suggests that we use the regularization term only along the z axis, that is,

$$\phi(h) = \beta \sum_{i,j,k} \varphi(h_{i,j,k} - h_{i,j,k-1}) = \beta \sum_{i,j} \sum_{k} \varphi(h_{i,j}(k) - h_{i,j}(k-1)) \quad (8)$$

with $\beta = \beta_z$, using the notation introduced in (2). The optimization problem is thus simplified to a sequence of 1D minimizations, namely, $\mathrm{h}_{i,j} = \arg\min_{\mathrm{h}} J_{i,j}(\mathrm{h})$, for every i, j, where

$$J_{i,j}(h) = \sum_{r=0}^{R-1} \|B^r h - \mathrm{l}^r_{i,j}\| + \beta \sum_{k} \varphi(h(k) - h(k-1)). \quad (9)$$

There exist many convergent iterative methods to calculate h. Based on a comparative study on the speed of convergence of different

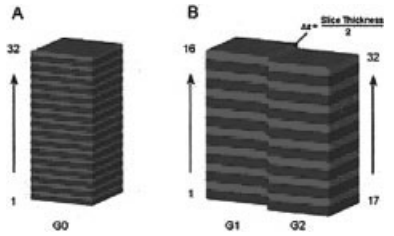

Figure 1. Acquisition of the different slices in a volume. (A) The slice acquisition sequence in the standard high- resolution dataset (G0). (B) The acquisition sequence in the slice-shifted low-resolution datasets (G1 and G2). [Color figure can be viewed in the online issue, which is available at www.interscience.wiley.com.]

minimization methods (Nikolova and Ng, 2001), we focus on the additive form of half-quadratic regularization (Aubert and Vese, 1997; Geman and Yang, 1995). This amounts to calculation of the solution at iteration n, say h^n, according to

$$\mathrm{h}^n = H^{-1}(2B^T \mathrm{l}_{i,j} + \beta D^T b_k^n),$$

where

$$H = 2B^T B + \beta D^T D$$

$$b_k^n = \begin{cases} 0 \quad \text{if} \quad |h^{n-1}(k) - h^{n-1}(k-1)| \le \alpha \\ h^{n-1}(k) - h^{n-1}(k-1) \\ \quad - \alpha \cdot \operatorname{sign}(h^{n-1}(k) - h^{n-1}(k-1)) \quad \text{otherwise} \end{cases}$$

$$\forall\, k = 1, \ldots, p.$$

It has been shown (Nikolova and Ng, 2003) that the sequence $\{\mathrm{h}^n\}$ converges to the sought solution $\hat{\boldsymbol{h}}$. Observe that the matrix H can be inverted only once, before starting the minimization for all i, j and that calculation of b_k^n is extremely simple.

IV. DATA ACQUISITION

A. The Adapted fMRI Sequence. One approach to obtain high-resolution MR images is to acquire different 3D volumes (Roullot et al., 2000) before applying a super-resolution reconstruction technique. Unfortunately most 3D acquisition procedures cannot reach the required temporal resolution necessary for fMRI experiments, so that fMRI brain volumes have to be acquired as a stack of parallel 2D slices as illustrated in Figure 1(A). To obtain two different sets of low-resolution shifted volumes, the standard fMRI acquisition protocol is adapted. The two volumes are acquired in an interleaved fashion where the first volume (G1) is positioned with a relative slice offset equal to zero, and the second volume (G2) with a relative slice offset (Dz) of half the slice thickness, as is shown in Figure 1(B).

B. Slice-Shifted Acquisition.

Morphological Data. Structural MR images of an apple were acquired on a clinical whole-body 1.5 T Siemens Sonata MR scanner. The high-resolution volume (ground truth) and the low-resolution slice-shifted volumes were all acquired consecutively with a standard TSE sequence, with the following acquisition parameters: TR/TE = 3300 ms/12 ms, turbo factor = 5, high-resolution voxel size = 1 × 1 × 1 mm and low-resolution voxel size = 1 × 1 × 2 mm, respectively. The acquisition time of the high-resolution volume was 46 min and the acquisition time of each of the two slice shifted volumes was 23 min, resulting in an equal total acquisition time.

Functional MRI Data. To validate the super-resolution technique with fMRI datasets, simulated and real fMRI datasets were used.

In the real fMRI datasets a visual stimulation paradigm for retinotopic mapping was used. The stimuli used were designed to stimulate the horizontal (HM) and vertical (VM) visual field meridian, using horizontally and vertically oriented wedge-shaped checkerboards alternating at 4 Hz. The HM and VM stimuli were alternated in blocks of 10 brain volume scans. In this experiment a total of 10 sessions of 12 blocks each, i.e., 120 scans per session, were performed on the same subject. During the experiment two different acquisition strategies were interleaved: the high-resolution fMRI (ground truth) acquisition protocol and the low-resolution (slice-shifted) fMRI acquisition protocol, yielding 5 high-resolution (ground truth) and 5 slice-shifted low-resolution volume datasets. In the slice-shifted mode the slice thickness was doubled as compared to the standard sequence. The two shifted volumes were acquired consecutively, with the first volume at a relative position of 0 mm and the second volume shifted in slice position over a distance equal to the slice thickness of the high-resolution images (Fig. 1).

The data were collected on a Siemens Sonata 1.5T MR system using a FE-EPI sequence (TR/TE = 3328 ms/54 ms, voxel size = 2 × 2 × 2 mm for the ground truth images and 2 × 2 × 4 mm for the slice-shifted images, acquisition matrix = 128 × 128). The global acquisition time of the two different slice-shifted volumes (acquisition time for one slice shifted volume = 1664 ms) acquired in an interleaved fashion was set equal to that of one high-resolution volume (acquisition time = 3328 ms). Thus after postprocessing 120 super-resolution volumes were generated with an effective TR of 3328 ms in every session, equaling the number of high- resolution volumes in a session.

In general, it is very difficult to rank the performances of the super-resolution interpolation techniques in a qualitative analysis of the real fMRI data. Therefore we created a synthetic dataset with known activated areas inserted, to obtain a more objective measurement of which super-resolution algorithm yields the best results in the activation maps. This synthetic dataset was generated with Matlab (Release 13, The Mathworks Inc.) routines: The mean EPI MR volume was used as a template with a base resolution of 3 × 3 × 4 mm^3. This template was duplicated 120 times to generate a dynamic time series, with different "activated regions" inserted in an interleaved mode of 10 "rest" volumes and 10 "activated" volumes. These "activation" regions consisted of different spheres with different radii and an irregularly shaped area at carefully chosen positions. The intensity of activation was set to a maximum of 8% peak signal change. Two slice-shifted low-resolution datasets were generated by addition of the adjacent slices of the high-resolution dataset. Gaussian noise was inserted with a standard deviation of 2% for the high-resolution set and 1% for the low-resolution volumes.

V. GENERATION OF SUPER-RESOLUTION DATASETS AND fMRI ANALYSIS

A. Generation of the Super-resolution Datasets. The super-resolution datasets were generated using the algorithms described in section 3. Optimization of the minimizer h of the penalized objective function of Eq. (5) in the three spatial directions are denoted as 3D anisotropic filtering; on the other hand, optimization

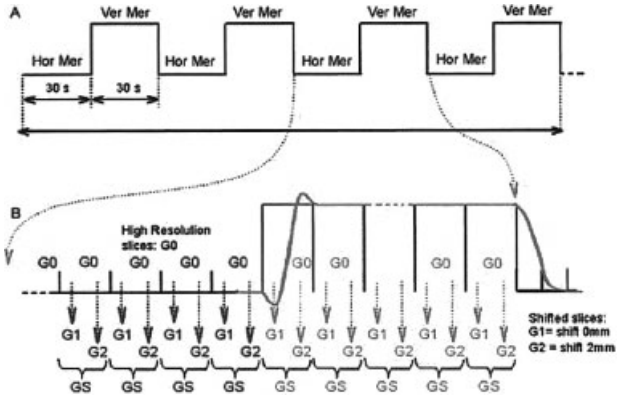

Figure 2. The two different acquisition protocols for the visual paradigm: high-resolution (G0) and slice-shifted low- resolution (G1 and G2 for the non-shifted and the shifted slices, which are interpolated to a new super-resolution dataset GS). In (a) the entire stimulation paradigm is shown and in (b) two consecutive blocks are shown in detail. The expected hrf function in the activated voxels is drawn on top of these blocks. Notice the loss of temporal information in the super-resolution dataset. (G0, G1, G2 as defined in Fig. 1.) [Color figure can be viewed in the online issue, which is available at www.interscience.wiley.com.]

in the slice direction only using Eq. (9) is called 1D anisotropic filtering. In the results we also show and compare interpolated datasets obtained with some simple interpolation techniques. The first consists of combining the two low-resolution datasets together to one new dataset by using the slices of the nonshifted low-resolution dataset as the odd slices and those of the shifted low-resolution dataset as the even slices of the newly generated dataset. This resulting dataset is denoted as the "composed" dataset. A second simple technique is to compute the average of all the low-resolution voxels containing the wanted high-resolution voxel; the resulting interpolated dataset is called the "average" dataset.

B. Postprocessing of the fMRI Data. Postprocessing of the functional MR images was performed with the aid of a number of procedures, which are all implemented in the standard SPM99 package (Friston et al., 1995). First, the dataset was spatially preprocessed by motion correction and spatially smoothed with an isotropic Gaussian kernel of 3 mm. These preprocessing steps were identical for both the high-resolution reference data and the low-resolution shifted datasets used to generate super-resolution datasets with the algorithm described above. In the synthetic dataset no preprocessing was performed.

After these preprocessing steps the actual statistical analysis was performed on the different datasets (synthetic and real). As a result of the loss of temporal information in the slice-shifted acquisition mode of the data, it was not possible to use standard SPM fMRI statistical analysis protocols for the super-resolution datasets. Figure 2 displays the haemodynamic response function (hrf) and the acquisition protocol for the stimulation paradigm and clearly demonstrates that the image data acquired during the initial and final portion of the hrf are not in a stationary state (plateau), and thus cannot be used for the post hoc super-resolution algorithm, which should combine two sets of shifted and nonshifted volumes acquired with an identical neurophysiological response condition. Instead, we generated an fMRI design matrix using the boxcar function, without convolving it with the hrf, and we discarded the first image volumes (G0 for the high resolution, and G1 and G2 for the low resolution) of every condition acquired during the nonstationary state of the haemodynamic response (Fig. 2). As a result of this adaptation, the analysis technique assumed a block model without convolution with the hrf, which is not as powerful as the standard fMRI analysis using the hrf model. Therefore, to compare the different acquisition protocols, we also analyzed the high-resolution reference datasets, both with the standard fMRI statistics toolbox (boxcar response convolved with hrf) and with the adapted simplified statistics toolbox (boxcar response only), using SPM. The super-resolution datasets, on the other, hand, were analyzed only with the simplified design matrix in SPM. (The results of the simplified statistics for the high-resolution datasets are not shown in the activation maps, but are reported in the corresponding tables and graphs.)

V. RESULTS

A. Morphological Data.

Qualitative Analysis. In Figure 3 we visually compared the resulting datasets of the apple generated with the super-resolution algorithms, the original reference high-resolution dataset and the original low-resolution datasets. In panel 3(A) the slices of the volume are displayed in the acquisition plane; in 3(B) and 3(C) slices are shown perpendicular to the acquisition plane. From 3(A) we can conclude that, in the acquisition plane, the reconstructed images look very similar, displaying a higher SNR compared to the high-resolution reference image (left top image). This is what we expect because the in-plane resolution for the original low-and high-resolution images were identical. Note that the 3D anisotropic filtered image displays a much higher SNR, compared to the other images, which is a result of the contribution of the anisotropic diffusion regularization term in smoothing the images in three dimensions.

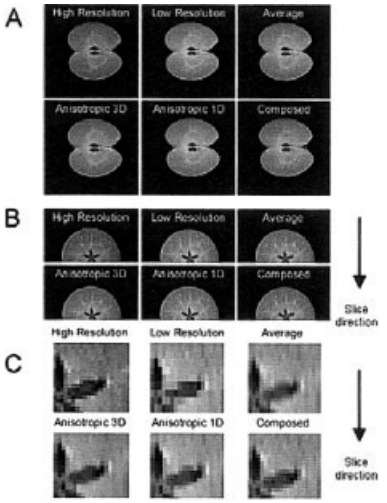

Figure 3. Transversal (A) and coronal (B) views of the different reconstructed images of the apple dataset. The first two slides in each panel display the native high-and low-resolution images. The other slides show reconstructions obtained with the different interpolation techniques: average, anisotropic 3D, and 1D, and composed. In the coronal view improvements in slice direction are displayed in the transversal view the in-plane effects are demonstrated. (C) shows close-up views of coronal slices of the different reconstructions.

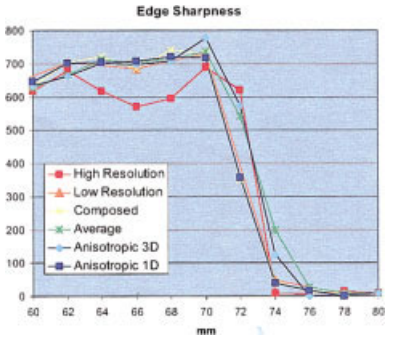

Figure 4. Measured edge sharpness of the different datasets in the direction perpendicular to the imaging plane.

In the slices cut perpendicular to the acquisition plane [Figs. 3(B) and (C)] we observe in the original low-resolution images artifacts at the object edges compared to the high-resolution reference images, as a result of the larger slice thickness of the low-resolution images. These artifacts are clearly reduced in the interpolated images. Careful inspection shows that both diffusion filtered superresolution images (anisotropic in 3D and in 1D) preserve best the structure of the apple, whereas the composed and average images behaved less well.

Edge sharpness of the images, another quality criterion for the super-resolution algorithms was also evaluated. Cuts of the different reconstructions in the neighborhood of a sharp intensity variation in the slice direction were compared and shown in Figure 4. It is seen that the 1D anisotropic reconstruction technique is capable of the sharpest edge reconstruction, whereas the other reconstructed datasets display a clear loss in edge sharpness. To quantify these results, we used the mathematical formula suggested by Greenspan et al. (2002) to estimate this edge width (Table I). From this it appears that the anisotropic reconstruction technique is capable of a sharp edge reconstruction.

To demonstrate the edge reconstruction capability we also analyzed the 1D synthetic data by generating the different reconstructed datasets from the two subsampled "low-resolution" signals with and without the inserted noise (Fig. 5). This figure demonstrates the superiority of the anisotropic reconstruction technique. In panel 5(A) the anisotropic reconstructed signal clearly overlaps with the original signal, and the other have a large error at the sharp boundaries; in 5(B) with the noise inserted the deviation of the signal from the anisotropic reconstructed is still much less than those of the other reconstructions. The deviations of the signals from the original are displayed in 5(C) and (D), respectively, for the noiseless and the noisy case.

Table I. Measured edge width in the different datasets of the apple with the method proposed by Greenspan.

High	6.45
Low	9.6
Composed	5.85
Average	5.95
Anisotropic 3D	5.75
Anisotropic 1D	5.73

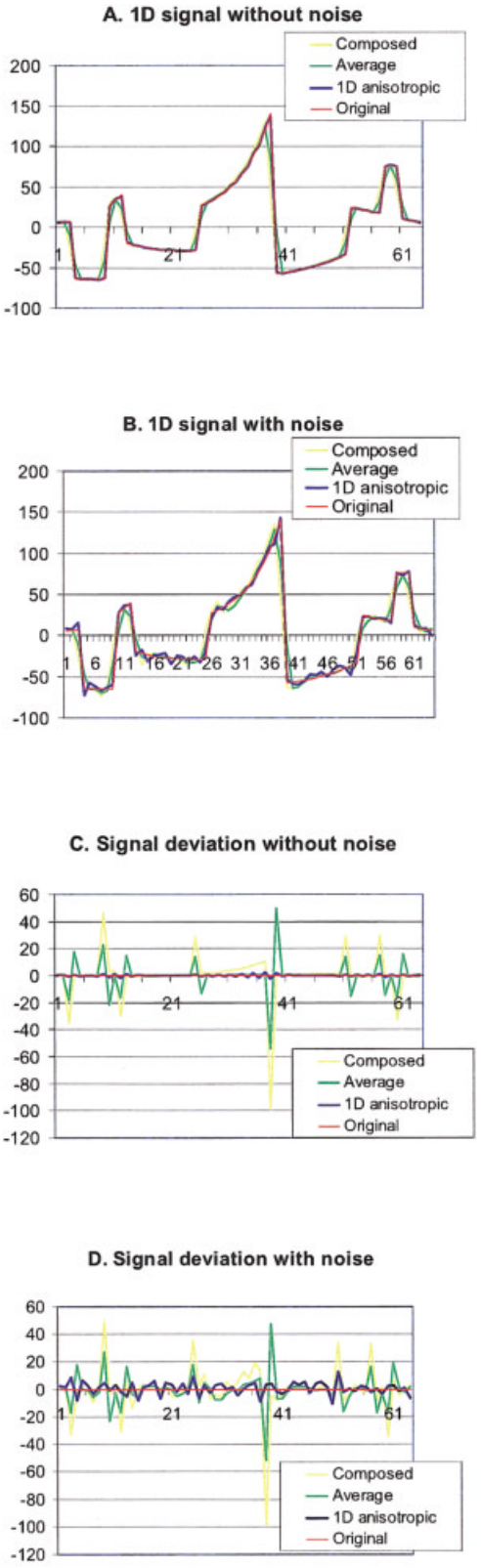

Figure 5. Signal time traces of the 1D synthetic signal and their different reconstructions. The red line displays the original signal, the yellow line the composed, the green the average, and the blue line the 1D anisotropic reconstructed signal. In 5A the signals are reconstructed from the "low-resolution" signals without and in 5B with random noise added, 5C and D show respectively the deviations of the reconstructed signals from the original signal.

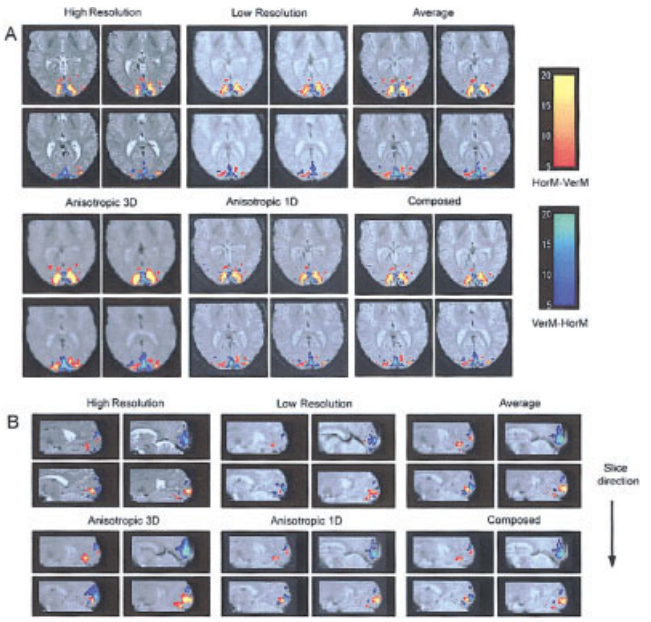

Figure 6. Slices of activated areas resulting from the visual stimulation paradigm overlaid on the mean EPI images for the different datasets. In A, slices are displayed in the transversal acquisition plane; in B, sagittal slices are shown. Two different color bars are used, in both the *t*-value threshold ranges between 5 and 20. The red-to-yellow bar presents the horizontal meridian stimulation against the vertical meridian stimulation and the blue-to-green bar presents the vertical meridian against horizontal meridian stimulation.

B. fMRI Data.

Qualitative Analysis. To analyze the fMRI data we generated SPM activation maps, displaying the activated areas above the statistical threshold (pcorr <0.05), overlaid on the mean EPI slices of the interpolated datasets. Figure 6(A) displays activation images of the retinotopic mapping fMRI experiment in the acquisition plane with the corresponding activation superposed, and 6(B) shows those perpendicular to the slice direction.

Globally the activation maps of the interpolated datasets are largely similar to those of the high- resolution reference dataset. A closer look at the data, however, reveals that the 1D and 3D anisotropic super-resolution datasets show higher *t* values at the foci of the activated areas than the reference high-resolution, the original low-resolution, and the average and composed datasets. Also the size of the activated clusters with a *t* value above threshold appears to be larger in the super-resolution datasets compared to the original data. When comparing the two different super-resolution datasets (3D vs 1D anisotropic regularization), we observed the following differences. The 3D anisotropic images display more intense but less sharp activation patches than the 1D anisotropic interpolated and high-resolution datasets both in- and through-plane. The 1D anisotropic super-resolution dataset demonstrates a higher resolution of the activated patches in the slice direction than the low-resolution dataset and the 3D super-resolution anisotropic dataset. These smoothing effects are the result of the larger smoothing inherent to the 3D anisotropic interpolation algorithm in all directions.

The same statistical analysis was performed on the synthetic dataset. Here we observe similar results as with the real fMRI datasets. Both anisotropic super-resolution datasets show activated areas matching the activated areas inserted into the datasets, as seen in Figure 7.

Quantitative Analysis. To measure the performance of the interpolation algorithms in a more objective way, we quantified some aspects of the results. For this, the following quantitative measurements were performed: (1) the highest global *t* score value observed in the activated areas and (2) the activated volume above the pcorr value of 0.05 across all remaining clusters larger than 10 voxels. The results of these measurements are displayed in Figures 8(A) and (B). In Figure 8(A) the largest observed *t* value in the activated areas is measured for the horizontal meridian stimuli against the vertical meridian stimuli. The super-resolution datasets generated higher maximal *t* values than the high-resolution reference data set and the original low-resolution datasets. In Figure 8(B), the activated volume above threshold is plotted for all datasets. Again we observe that both interpolated datasets generated a much larger total volume of activation above threshold and that the dataset generated with the 3D anisotropic diffusion algorithm retains the largest volume of activation above threshold. Therefore these quantitative measurements suggest that the 3D anisotropic super-resolution dataset is the one yielding both the largest significance and largest detectability of the activated areas.

For the synthetic dataset, on the other hand, we measured the capability of the super-resolution techniques to separate two closeby activated areas. Figure 9 shows line graphs of the calculated t-values of a cut in the slice direction through two activated regions, with a separation of 2 slices in panel 9(A) and 1 slice in Figure 9(B). These results demonstrate that both super-resolution algorithms show a good separation of the activated areas, which closely resembles the separation observed in the high-resolution dataset. This separation of distinct activated areas is also much better than that in the low-resolution, average, and composed datasets.

VI. DISCUSSION AND CONCLUSION

In this work we investigated the possibility of using super-resolution postprocessing techniques in conjunction with an appropriate acquisition protocol to increase the spatial resolution of fMRI studies when thin-slice acquisition is restricted by hardware considerations.

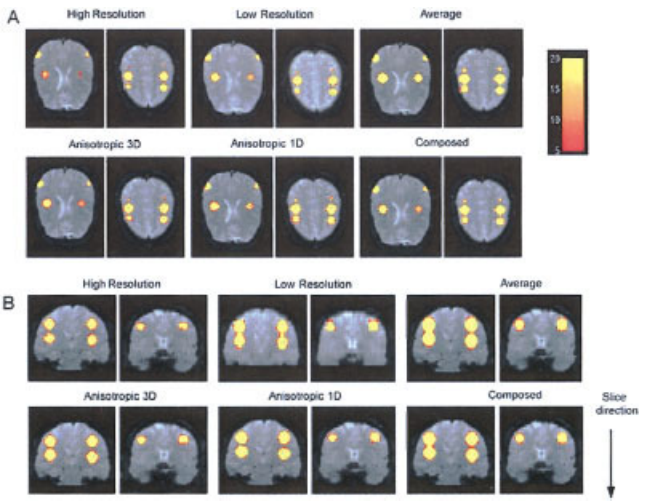

Figure 7. Comparison between the "activated" areas observed in the high, low, and interpolated datasets for the synthetic data. In A, slices are displayed in the transversal plane; in B, sagittal slices are shown. The activated areas are overlayed on the mean EPI image with a color range from red to yellow.

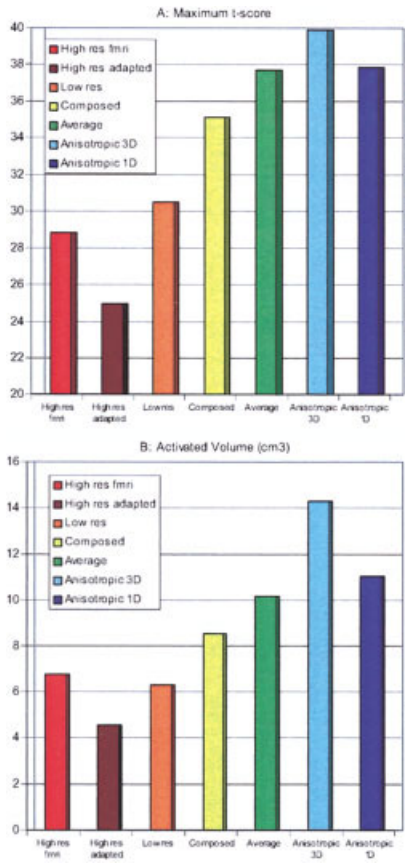

Figure 8. Bar graph of the largest *t*-value in the activated areas (A) and the total activated volume above the pcorr threshold of 0.05 (B), for the high-resolution dataset, the low-resolution dataset, and the different interpolated datasets in the visual retinotopic mapping experiment.

We proposed a reconstruction method based on a minimization algorithm with a constraint term on the smoothness of the solution. Two kinds of constraints have been tried: either penalize the intensity gradient in three dimensions (usually employed for image restoration), or only in the slice direction as imposed by the acquisition protocol. To evaluate the performance of these techniques we compared the super-resolution images and the reference "golden standard" high-resolution images for real morphological, real and synthetic fMRI data. From the morphological data we conclude that the use of the super-resolution technique improves the signal-to-noise ratio (SNR) compared to both the high-resolution reference images and the original shifted low-resolution images, which was also observed in other studies (Greenspan et al., 2002). With respect to image sharpness, the reconstructed super-resolution images displayed a closer resemblance with the reference high-resolution dataset than the original low-resolution data did, as demonstrated both on the morphological and synthetic 1D data.

In the fMRI experiments on human volunteers a gross resemblance is observed between the observed activated areas in the high-resolution dataset and the superresolution datasets. In the synthetic datasets, identical observations were made, with both the 1D and 3D anisotropic datasets demonstrating activated areas in good agreement with the position and the size of the simulated activated areas. Quantitative analysis demonstrated a superiority of the 1D and 3D anisotropic super-resolution datasets compared to the other data reconstruction techniques in terms of statistical significance of the observed activated areas. The ability of these super-resolution algorithms to separate different activated areas was also shown to be comparable to the high-resolution reference dataset and to be much better than the other combination techniques as is demonstrated in the synthetic experiment.

As a result of the inherent characteristics of the MR imaging technique, the super-resolution techniques could only be employed in the slice direction. The in-plane image data of a single slice are generated by a 2D Fourier transform of the acquired set of MRI time-domain signals. As a consequence, the use of the super-resolution algorithms in the image space can only be beneficial in the slice direction (direction perpendicular to the image plane), because shifted slices correspond to different parts of the object in the image space. In-plane shifting, to increase the "in-plane" resolution in the image space, does not add any new information due to the properties of the 2D inverse Fourier transform used in MR imaging (Scheffler, 2002). In-plane shifting is indeed nothing other than a global phase shift in the acquisition space (k-space), the original temporal domain, which does not affect the inherent spatial frequency resolution of the acquired data. In other words: increasing the "in-plane" resolution by in-plane shifting of the image is equivalent to zero-padding of the raw data in the temporal domain (Greenspan et al., 2002).

A major drawback of these super-resolution reconstruction techniques is the loss of temporal resolution, which is inherent to the

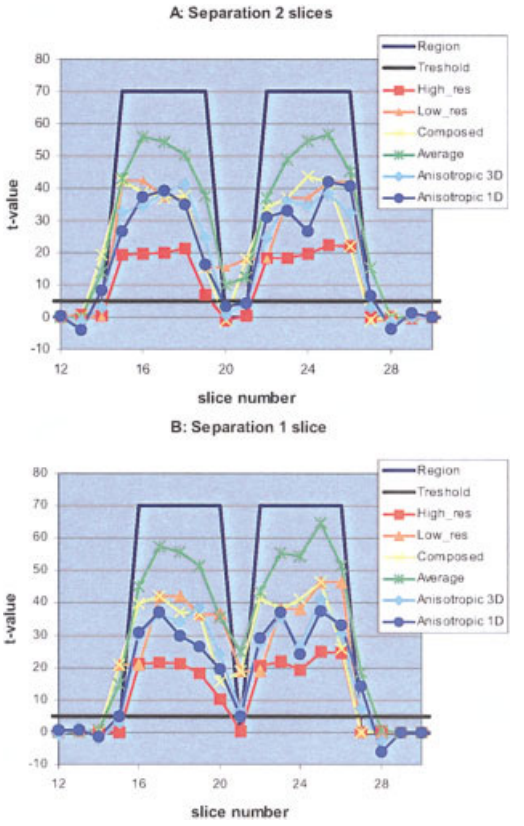

Figure 9. Line graphs of a cut in the slice direction showing the *z*-score values for activated areas separated by 2 slices (A) and 1 slice (B) for the different reconstructions. The real boundaries of the activated areas are shown with a dark blue line.

combination of two datasets acquired at different time points. Therefore one is no longer able to correctly visualize rapidly changing signal intensities in the activated brain. To circumvent this problem and minimize artefactual signals, we opted in this case to remove the transient phases of the haemodynamic response in the fMRI signal at the beginning of each block of different brain activation and only use those MR images acquired during a steady state of brain activity. This solution, however, is not feasible in event-related studies where intrinsically no steady state of activation does exist. In these experiments a possible solution could be to change the signal intensity of the different slice shifted datasets to correct them for their individual acquisition time. This can be done by interpolating the time trace of the fMRI signal for every voxel of the slice-shifted dataset to the same data time points of the nonshifted dataset (Henson et al., 1999).

When comparing the activation maps of the super-resolution datasets, we found that the 3D penalization of the gradient results in a loss of sharpness in several activated patches as compared to the 1D case. Taking into account the results of the real and synthetic datasets, we conclude that, although the 3D anisotropic diffusion superresolution dataset displays the largest activated areas and highest t values, it is much more smoothed than the 1D anisotropic super-resolution dataset. Therefore the latter type of algorithm is the better choice if one wants to detect small activated areas with a high resolution, which we suggest to apply in fMRI work together with the commonly used 3D local Gaussian smoothing before the SPM calculation, which will result in an isotropic distribution of the noise in the images necessary for the SPM statistics.

To conclude, this study demonstrates the applicability of super-resolution reconstruction techniques in functional MR imaging to increase the slice resolution of the acquired images and of the resulting activation maps. The anisotropic (1D and 3D) super-resolution interpolation techniques proposed have been proven to be capable of augment in the resolution of the images without the loss of SNR and to display the expected activated areas in fMRI studies.

REFERENCES

K. Aizawa, T. Komatsu, and T. Saito. Acquisition of very high resolution images using stereo cameras, SPIE Visual Communi Image Process 1605 (1991), 318–328.

G. Aubert and P. Kornprobst, Mathematical problems in image processing: partial differential equations and the calculus of variations, Springer-Verlag, New York, 2002.

G. Aubert and L. Vese, A variational method in image recovery. SIAM J Num Anal 34 (1997), 1948–1979.

D. Capel and A. Zisserman. Super-resolution enhancement of text image sequences, Proc Int Conf Pattern Recogni (2000), 600–605.

W. Chen, K. Ugurbil, High spatial resolution functional magnetic resonance imaging at very- high-magnetic field, Top Magn Reson Imaging 10 (1999), 63–78.

M. Elad and A. Feuer, Super-resolution reconstruction of continuous image sequence, IEEE Trans-on Pattern Analysis-and Machine Intell 21, (1999), 817–834.

H. Engl, M. Hanke, and A. Neubauer, Regularization of inverse problems, Mathematics and its Applications, Kluwer Academic, Boston, 2000.

H. Fischer, R. Ladebeck, Echo-planar imaging image artefacts, In F.A. Schmitt, M. Stehling R. Turner, Eds., Echo-planar imaging, theory, technique and Application, Springer Verlag: Berlin, 1998, 191–200.

K.J. Kriston, A.P. Holmes, J.B. Poline, P.-J. Grasby, S.C. Williams, R.S. Frackowiak and R. Turner, Analysis of fMRI time-series revisited, Neuroimage 2 (1995), 45–53.

D. Geman and C. Yang, Nonlinear image recovery with half-quadratic regularization, IEEE Trans Imag Process 4 (1995), 932–946.

H. Greenspan, G. Oz, N.-Kiryati, and S. Peled, MRI inter-slice reconstruction using super-resolution, Magn Reson Imaging 20 (2002), 437–446.

R.N. Henson, C. Buechel, O. Josephs, and K. Friston, The slice-timing problem in event-related fMRI, Neuroimage, 9 (1999), 125.

F.G. Hoogenraad, M.B. Hofman, P.J. Pouwels J.R. Reichenbach, S.A. Rombouts, and Haacke, Sub-millimeter fMRI at 1.5 Tesla: correlation of high resolution with low resolution measurements, J Magn Reson Imaging 475–482.

M. Irani and S. Peleg, Motion analysis for image enhancement: resolution, occlusion, and transparency, J Visual Communi Image Represent 4: (1993), 324–335.

D.A. Kelley, J.E. Schenck. Very-high-field magnetic resonance imaging: instrumentation and safety issues. Top Magn Reson Imaging 10 (1999), 79–89.

M. Nikolova and M. Ng, Fast Image reconstruction algorithms combining half-quadratic regularization and preconditioning, Proc Int Conf Image Process Soc (2001), 277–280.

M. Nikolova, and M. Ng, 2003. Analysis of half-quadratic minimization methods for signal and image recovery. CMLA, Tech Rep 2003-15, Ava CMLA. UMR 8536-ENS, Cachan, France.

S. Peled and Y. Yeshurun, Superresolution in MRI: application to human white matter fiber tract visualization by diffusion tensor imaging, Magn Reson Med 45 (2001), 29–35.

E. Roullot, A. Herment, M. Bloch, M. Nikolova, and E. Mousseaux. Regularized reconstruction of 3D high-resolution magnetic resonance images from acquisitions of anisotropically degraded resolutions. Proc Int Conf Image Process pp. 3 (2000), 350–353.

L. Rudin, S. Osher, and E. Fatemi, Nonlinear total variation based noise removal algorithms. Physica D 60 (1992), 259–268.

K. Scheffler, Superresolution in MRI? Magn Reson Med 48 (2002), 408.

K.R. Thulborn, S.Y. Chang, G.X. Shen, and J.T. Voyvodic, High-resolution echo-planar fMRI of human visual cortex at 3.0 tesla, NMR Biomed 183–190.

J. Xiong, P.T. Fox, and J.H. Gao, The effects of k-space data undersampling and discontinuities in keyhole functional MRI Magn Reson Imaging 109–119.

M. Zaitsev, K. Zilles, and N.J. Shah, Shared k-space echo planar imaging with keyhole, Magn Reson Med 45 (2001), 109–117.